Robust and efficient hybrid molecular electroanodes for water oxidation based on coordination oligomers

Md Asmaul Hoque,[1,+] Marcos Gil-Sepulcre,[1,+] Adiran de Aguirre,[1] Johannes A. A. W. Elemans,[2] Dooshaye Moonshiram,[3] Roc Matheu,[1] Yuanyuan Shi,[4] Jordi Benet-Buchholz,[1] Xavier Sala,[5] Marc Malfois,[6] Eduardo Solano,[6] Joohyun Lim,[7] Alba Garzón-Manjón,[7] Christina Scheu,[7] Mario Lanza,*[,4] Feliu Maseras,*[,1,5] Carolina Gimbert-Suriñach,*[,1] and Antoni Llobet*[,1,5]

[1]Institute of Chemical Research of Catalonia (ICIQ), The Barcelona Institute of Science and Technology (BIST), Avinguda Països Catalans 16, 43007 Tarragona, Spain.

[2]Institute for Molecules and Materials Radboud University, Heyendaalseweg 135- 6525AJ, Nijmegen, The Netherlands.

[3]Instituto Madrileño de Estudios Avanzados en Nanociencia (IMDEA-Nanociencia), Calle Faraday, 9, 28049 Madrid, Spain.

[4]Institute of Functional Nano & Soft Materials (FUNSOM), Collaborative Innovation Center of Suzhou Nanoscience and Technology, Soochow University, 199 Ren-Ai Road, 215123 Suzhou, China.

[5]Departament de Química, Universitat Autonoma de Barcelona, 08193 Cerdanyola del Valles, Barcelona, Spain.

[6] NCD-SWEET beamline, ALBA synchrotron light source. Carrer de la Llum 2-26, 08290 Cerdanyola del Vallès, Barcelona, Spain

[7] Max-Planck-Institut für Eisenforschung GmbH, Max-Planck-Strasse 1, 40237 Düsseldorf

+ These authors have equally contributed to this work

Abstract

Linear coordination oligomers with controlled chain lengths based on a Ru water oxidation catalyst and a bidentate linear bridging ligand have been prepared and characterized for the first time. These new oligomers have an extraordinary capacity to adsorb on graphitic surfaces thanks to a multiple perpendicular CH-π type of bonding between the auxiliary ligands bonded to Ru metal center and the hexagonal rings of the graphitic surfaces. The strength of this interaction increases as the number of units increases due to a larger enthalpy associated with the increasing number of CH-π interactions, as opposed to a nearly constant unfavorable entropic factor. The CH-π interactions also provide for an additional stabilization factor due to their reversible formation and breaking. Further these new hybrid materials behave as *molecular electroanodes* that catalyze the water oxidation to dioxygen reaction at pH 7, reaching unprecedented performance in terms of current densities.

Graphical abstract
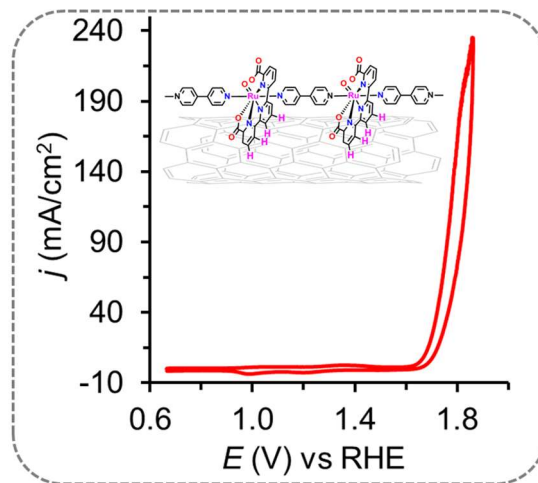
Introduction

Molecular water oxidation catalysts (WOCs) have experienced a large development over the last decades[1,2,3,4] reaching turnover frequencies (TOF) in the range of 50.000 s^{-1}, which is about two orders of magnitude higher than nature's light induced oxygen evolving complex in photosystem II (OEC-PSII) that turns in the millisecond time scale.[5,6] This has been achieved thanks to the synthetic versatility of molecular transition metal complexes where the first and second coordination sphere of the metal center can be tuned so that it can exert supramolecular interactions, hydrogen bonding effects, local acid-based enhancements, etc.[7] Further, redox active ligands can also share the storing of oxidative equivalents together with the metal center and the oxo group.[8] On the other hand, metal oxide-based catalysts have also experienced a large improvement over the past years thanks to the fine tuning of particle size and morphology that strongly influence their performance.[9,10,11,12,13]

Despite their versatile and modular properties, the generation of electroanodes and cathodes for water splitting devices based on molecular complexes anchored onto solid surfaces has received far less attention than conventional non-molecular materials. Nevertheless, a few examples exist in the literature where molecular water oxidation catalysts have been adequately modified with an anchoring functionality and anchored them onto conductive or semiconductive solid surfaces with varying degrees of performance and stabilities.[14,15,16,17,18,19,20,21,22,23] Promising strategies halfway between the anchoring of a molecular catalyst at a surface and metal oxides, include the partial use of surface atoms as ligands for the first coordination sphere of the metal center and single atom site isolation, that have been reported recently for the water oxidation reaction and others.[24,25]

The key critical parameters for predicting and understanding the performance of molecular water oxidation catalysts anchored onto a conductive surface are the mechanism of O-O bond formation[26] and the functionality that links the catalyst to the surface.[27] One of the most successful examples in terms of turnover numbers (TONs) and robustness is [Ru(O)(tda)(pyp)$_2$], **1-O-pyp**, (tda = [2,2':6',2''-terpyridine]-6,6''-dicarboxylato; pyp is 4-(pyren-1-yl)pyridine)) that is capable of achieving more than a million TONs without apparent associated deactivation reactions.[28] Modest current densities have however been achieved with molecular anodes in the range of 10 mA/cm^2 at pH 7 with an overpotential of about 400 mV at the foot of the catalytic wave.[28] The limiting factor to improve the absolute current densities here is due to the relatively small amount of catalyst that can be deposited at the surface of the electrode. On the other hand, water oxidation electroanodes based

on oxides can achieve current densities in the range of 0.2-1 A/cm^2,[29,30,31,32,33,34] that is the typical range of current densities operating in commercial electrolyzers.[35,36] The current density obtained in commercial electrolyzers is achieved by depositing a large amount of the catalyst oxide on top of the electrode surface thus generating a 3D electrode. However only around 0.1-1 % of the oxide deposited typically ends up being active, depending on the deposition methodology.[37,38] Furthermore, only a limited number of oxides are capable of acting as water oxidation catalysts under neutral conditions and their TOF values are generally much lower than those obtained with molecular catalysts.[39,40] Taking into account the benefits of molecular catalysts in terms of synthetic versatility and performance in comparisons to oxides, we aimed for the discovery of molecular catalysts that could potentially deliver large current density and be vastly and easily attached to electrode surfaces in a robust manner.

Here on we report new functional molecular coordination oligomers that can be strongly and massively adsorbed onto graphitic surfaces such as multiwalled carbon nanotubes (MWCNT), via aromatic catalyst-surface CH-π interactions. To the best of our knowledge, this anchoring strategy has never been described for molecular catalysts up to now. The resulting hybrid molecular material behaves as a rugged and powerful electroanode for the water oxidation reaction achieving unprecedented current densities for molecular catalysts in the range of 0.3 A/cm^2.

Results and Discussion

Synthesis of new coordination oligomers

Reaction of 1 eq. of [Ru(tda)(dmso)(H$_2$O)], with 1.5 eq. of the bridging ligand 4,4'-bypridine (4,4'-bpy) in MeOH:H$_2$O (1:1) generates a range of neutral oligomers of general formula {[Ru(tda)(4,4'-bpy)]$_n$(4,4'-bpy)} ranging from n = 1-4, as indicated in Scheme 1. From now on we will use the **n** value as the label for the corresponding oligomer or monomer. The oligomer with n = 4, **4**, is partially soluble within this reaction conditions and precipitates out of the solution. The oligomers **1-3** are on the other hand soluble and can be separated via column chromatography, allowing to obtain pure samples of **1** and **2**. However, we could not obtain pure samples of complex **3** possibly due to the low amount of this complex generated under the present reaction conditions. The 1:1.5 reaction ratio of [Ru(tda)(dmso)(H$_2$O)] and 4,4'-bpy in 2,2,2-trifluoroethanol (TFE) refluxed for 3 days generates oligomer **5**. On the other hand, the 1:1 reaction of [Ru(tda)(dmso)(H$_2$O)] and 4,4'-bpy in TFE generates a 1D linear oligomer **15**, with an average of 15 units together with the dimer {[Ru(tda)(dmso)]$_2$(μ-4,4'-bpy)}, **2'**, in a 2.6:1 ratio.
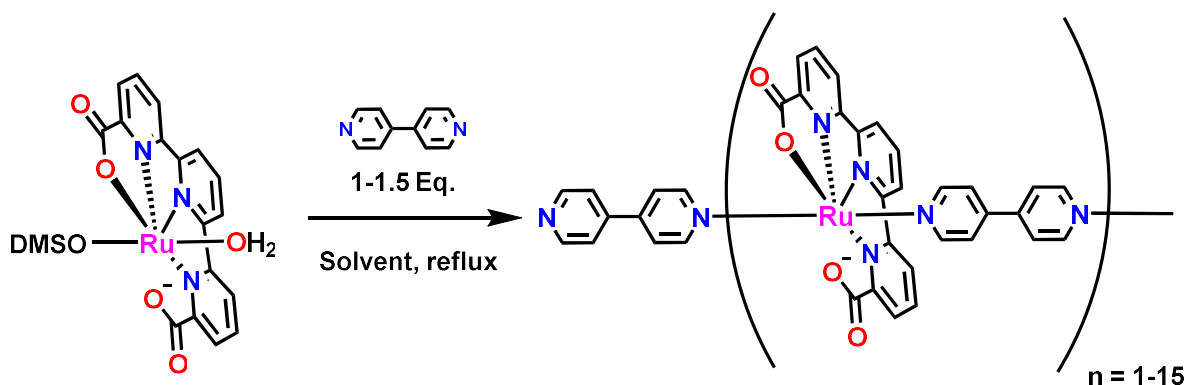
Scheme 1. Synthetic strategy for the preparation of {[Ru(tda)(4,4'-bpy)]$_n$(4,4'-bpy)} oligomers.

The characterization of these 1D oligomers and the monomer have been carried out by elemental analysis, mass spectrometry (Supplementary Figs. 14 and 15), UV-vis (Supplementary Fig. 16), X-ray absorption spectroscopy (Supplementary Fig. 32), powder and single crystal XRD (see Supplementary Figs. 17-19), Nuclear Magnetic Resonance (NMR) (Supplementary Figs. 4-8) and Diffusion-Ordered Spectroscopy (DOSY) (Supplementary Fig. 10). ^{1}H-NMR spectroscopy is especially useful since it not only allows us to assign all resonances that appear in the spectra but moreover

permits to calculate the average number of repetitive units of the synthesized oligomer. This is achieved by simple integration of key resonances as can be observed in Fig 1. Furthermore, DOSY experiments reflect the increasing volume of the polymer as the number of units grows (see Supplementary Fig. 10), but does not display a linear relationship due to the non-spherical shape of these molecules.[41,42] There is a number of coordination polymers that have been reported up to now using bridging ligands and transition metal complexes that resemble the oligomers just described here.[43] The main difference is that here we can not only control the number of units of the oligomer but we can also achieve a complete characterization of all of them both in solution and anchored in solid surfaces as will be described below.
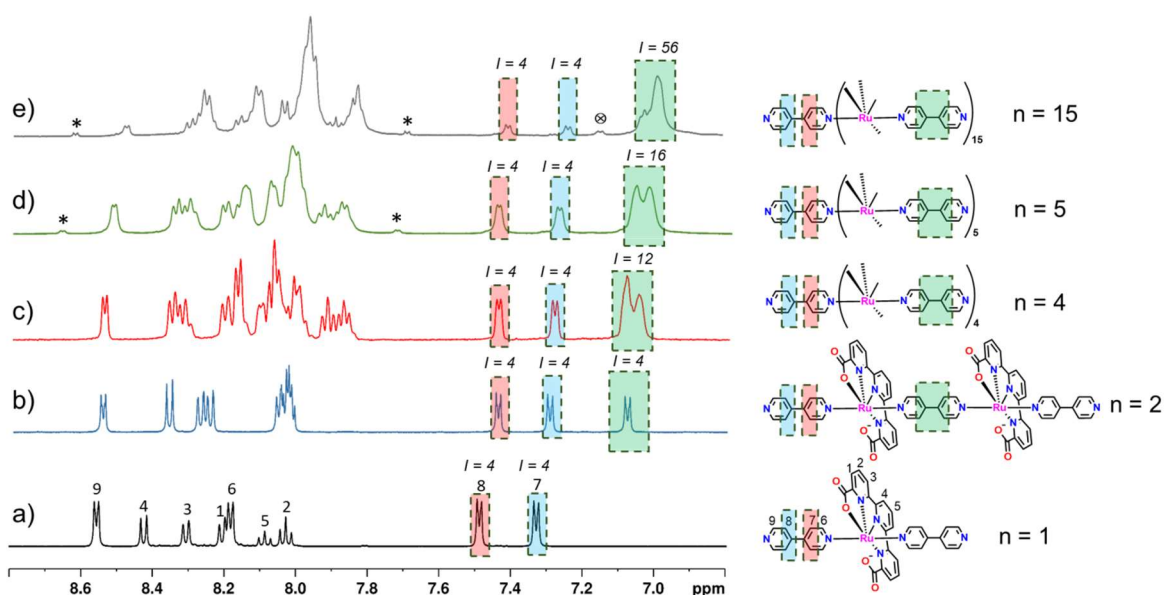

Fig. 1. Left, ^1H NMR spectra (500 MHz, 298 K, [d$_2$]-DCM/[d$_3$]-TFE (4:1)) for {[Ru(tda)(4,4'-bpy)]$_n$(4,4'-bpy)} oligomers. Right, drawing of the oligomers. The color shades relate to the assignment of key protons and their resonances. * indicates resonances for free 4,4'-bpy and $\otimes$ for **2'**.

Anchoring on graphitic surfaces via aromatic CH-π interaction

One of the most striking properties of this new family of coordination complexes is their capacity to strongly attach to graphitic surfaces in sharp contrast with their monomeric counterpart, **1**, which lacks any anchoring capability. The addition of a solution of coordination oligomers, **5** (See Supplementary Fig. 3) or **15** dissolved in TFE (1 mg of oligomer in 1 mL of solvent) to a solution of THF containing dispersed MWCNT, results in the immediate discoloration of the solution, indicating

the adsorption of **5** or **15** onto the MWCNT, which are labeled here as **5@CNT** and **15@CNT** respectively.

It is important to realize here that the typical catalyst anchoring based on oxides and/or coordination polymers consists on growing layers by electrodeposition or just by dropping a solution or a suspension of the material on the electrode. Oftentimes, an additional polymeric material as binder to further prevent mechanical deattaching is also added.[44] Thus, the process we describe here is radically different and is based on the strong affinity of oligomer **5** and **15** towards graphitic surfaces via multiple CH-π interactions.

Kinetics of the polymer desorption (see Supplementary Fig. 23) from glassy carbon electrodes (described below) monitored by Cyclic Voltammetry (CV), show that the rate of desorption decreases with increasing number of repetitive units. This together with the absence of affinity of the monomer [Ru(tda)(py)$_2$], **1-py**,[45] (py represents the monodentate pyridine ligand) suggests a synergic effect that correlates the strength of the interaction of the oligomers and MWCNT with the number of repeating units. This effect can be rationalized based on thermodynamic grounds as will be explained below.
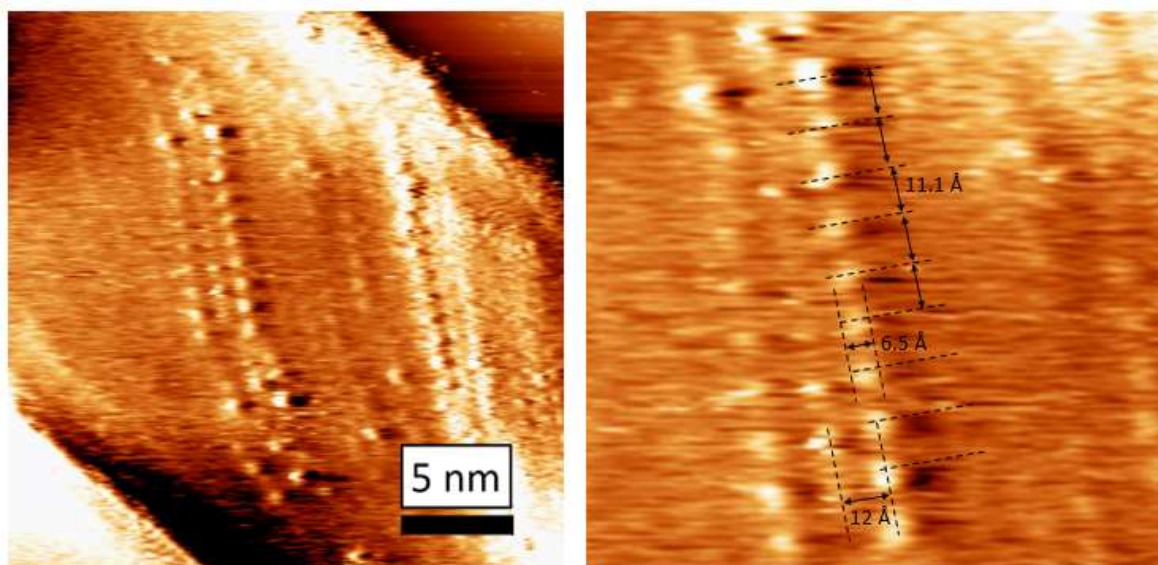

Fig. 2. Left, scanning tunneling microscopic (STM) image of **15** at the interface of highly oriented pyrolytic graphite (HOPG) and trifluoroethanol/dichloromethane/1-phenyloctane (50:50:1, v/v/v). Right, zoom in. The distances between two Ru-tda units in the polymer (11.1 Å), the distances

between two polymer chains (12 Å) and the size of a bright signature which corresponds to a Ru-tda unit (6.5 Å) are indicated. Tunneling parameters: V_{bias} = −248 mV, I_{set} = 170 pA.

A number of techniques including Scanning Tunneling Microscopy (STM), Scanning Electron Microscopy (SEM), Transmission Electron Microscopy (TEM) and Scanning Transmission Electron Microscopy (STEM) (Supplementary Figs. 36-40), ^{1}H-NMR (Supplementary Figs. 11-13), X-ray Absorption Spectroscopy (XAS) (Supplementary Fig. 32), X-ray Scattering (XS) (Supplementary Figs. 33-35), Resonance Raman spectroscopy (Supplementary Figs. 21 and 22), Thermogravimetric analysis (Supplementary Figs. 20) and electrochemistry in combination with DFT calculations were used to explore the nature of the interaction between the oligomers and the graphitic surfaces and only the most revealing experiments are described below while the rest of them are presented as Supplementary Information.

The interaction of the oligomers at the interface of highly oriented pyrolytic graphite (HOPG) and a droplet of a solution of the oligomers (0.5 mg/mL) in trifluoroethanol/dichloromethane/1-phenyloctane (50:50:1, v/v/v) were studied by STM. Figure 2, shows an STM image of immobilized oligomer chains. The bright signatures, which are associated with the Ru-tda fragments of the polymer, are separated by approx. 11.1 Å, which is close to the 11.4 Å calculated distance between to Ru centers linked by the 4,4'-bpy bridging ligands (see DFT analysis below) and that obtained from the single crystal X-ray structure of the dimer, **2** (see Supplementary Fig. 18). The 4,4'-bpy bridging ligands are not observed in the microscopy image, either due to the relatively small electron density associated with them or to their weak electronic coupling with the underlying surface. It is also interesting to see that the oligomers are aligned parallel to one another with an average oligomer-oligomer distance of about 12 Å, see Fig. 2. In aqueous media these neighboring oligomers will most likely interact to one another via hydrogen bonding between their carboxylate groups and water and thus influence the equilibrium between the catalytically active species and its precursors as will be further discussed in the next section. All these data point out to an interaction of the oligomers with the surface through the tda ligand that is situated perpendicular to the graphitic surface. Thus, the bonding occurs with the H atoms of the aromatic pyridyl rings of tda that interact with the π-system of the MWCNT generating multiple CH-π bonds.[46,47] The interaction of the CH groups of the tda ligand and the π system of the graphitic surface is simulated using the **1-py** monomer and a 4-(pyren-1-yl)butan-1-ol (Pyn-OH) molecule that can be considered a low molecular weight model of

10

graphite. Upon mixing both of them in d_6-DMSO the resulting ^{1}H-NMR spectra clearly shows a significant shift of some CH groups of the tda ligand and thus put forward the existence of these CH-π interactions (see Supplementary Figs 11-12). This is further supported by DFT calculations that visualize the same effect between **1-py** and pyrene. (see Supplementary Fig 13). Additional experiments to characterize the interaction of oligomer **5** and **15** were carried out using Grazing Incident Wide Angle X-ray Scattering (GIWAXS) techniques. Figure 3 shows the 2D GIWAXS patterns obtained for glassy carbon plate electrodes (**GC$_p$**) and for the oligomers **5** and **15** anchored on **GC$_p$**. As can be observed in the Figure, the **GC$_p$** presents an isotropic scattering ring whereas **5@GC$_p$** and **15@GC$_p$** display and anisotropic broad band. The latter, is associated with a preferential face on orientation of **5** and **15** on the **GC$_p$**,[48] which is in very good agreement with the results found not only for STM and NMR but also with the model proposed by DFT in Figure 4a discussed below. The 1D cuts displayed in Figure 3d, reveals a distance between the substrate and the **15** oligomer in the range of 3-6 Å (range 12-18 reciprocal space nm^{-1}), that perfectly agrees with the DFT model.

In order to further characterize these hybrid materials, DFT/MM calculations at the ONIOM (B97D:MM3:UFF) level,[49] were carried out to analyze the interaction of the oligomer with the graphitic surface. A data set collection of computational results is available in the ioChem-BD repository,[50] see Supplementary Information for QM/MM partition and further details. A 10-unit oligomer, {[Ru(tda)(4,4'-bpy)]$_{10}$(4,4'-bpy)}, **10**, was placed on a monolayer of graphene sheet composed of 2166 carbon atoms, and the structure was optimized in vacuum. The validity of the QM/MM partition was confirmed through calculations with an extended QM region, and the validity of the chemical model by introduction of a second layer of graphene, both reported in the Supporting Information.
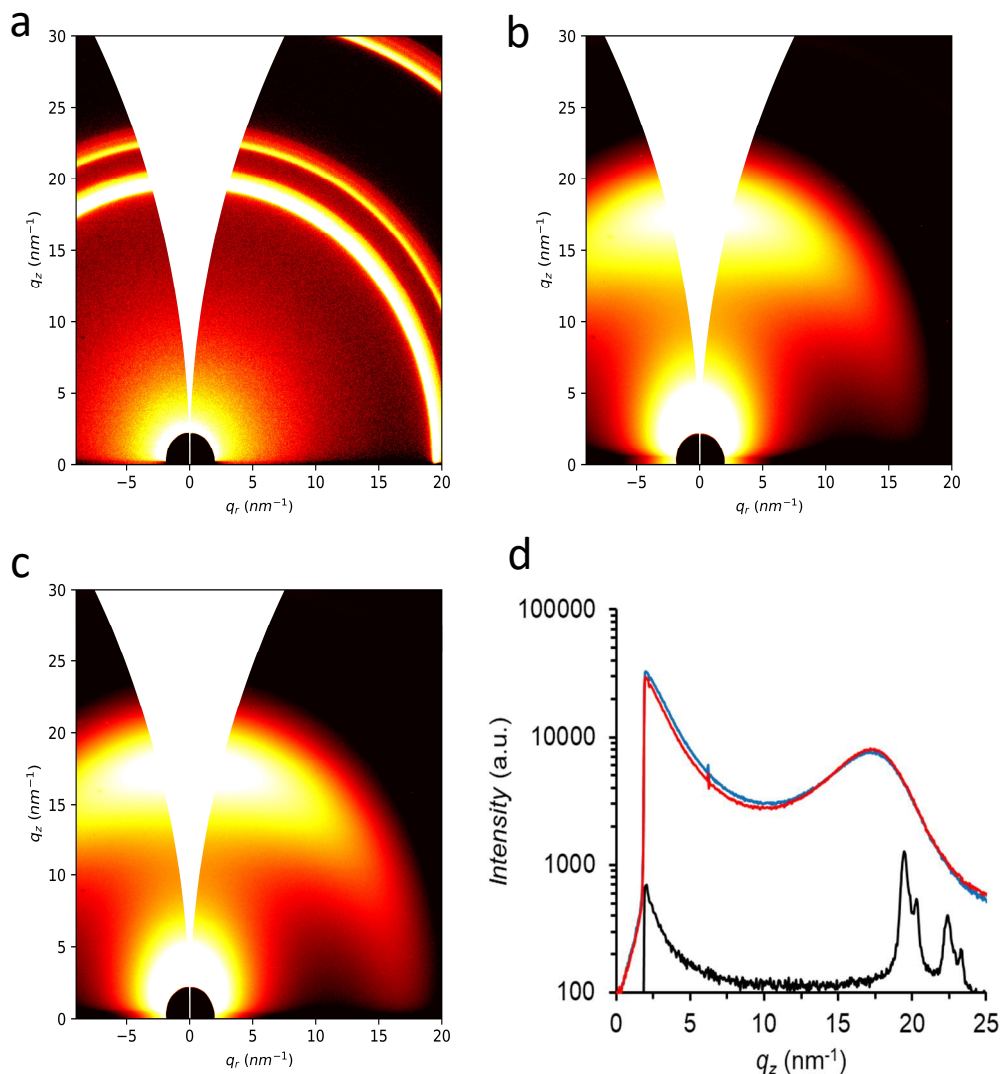
Fig. 3. Recorded 2D GIWAXS patterns of: (a) **GC$_p$**, (b) **5@GC$_p$**, (c) **15@GC$_p$** and (d) the corresponding q_z 1D cuts profiles near the specular direction. Black trace, **GC$_p$**; Blue trace **5@GC$_p$**; Red trace, **15@GC$_p$**.

The DFT obtained structure for **10** anchored on graphene is shown in Fig. 4a and is in very good agreement with the microscopy image. The Ru centers are situated in a mostly linear arrangement separated by 11.4 Å and interconnected with the 4,4'-bpy ligands that act as an axle while the tda ligands are threaded within this axle and situated perpendicular to it. The binding between the oligomer and surface consists of aromatic CH-π interactions. Four CH groups in each Ru monomer interact with the surface as shown in Fig. 4b, where the shorter H...C distances are between 2.74

and 3.03 Å, well within the expected range for C-H π interactions.[51] Out of these four CH groups, two come from the central ring of the tda ligand whereas the other two arise from one of the external pyridyl tda rings. Therefore, each tda ligand can bind in two isoenergetic symmetric ways as can be graphically observed in Fig. 4a, a fact that is further facilitated by the low energy rotation barrier of the Ru-N$_{pyridyl}$ bond. Figure 4c shows how the four CH groups of each tda ligand point out towards the center of a graphene six-member aromatic ring thus maximizing the strength of the CH-π bond. The computed energetics are especially interesting and informative as the Gibbs energy of binding between oligomer and surface is 133 kcal/mol, which can be decomposed into a binding enthalpy of 150 kcal/mol and an entropic penalty of 17 kcal/mol. Assuming that the binding enthalpy is additive, we can assign a value of *ca* 15 kcal/mol per Ru-tda unit (or an average of 3.75 kcal/mol per CH-π bond). The entropic penalty is mostly associated with bringing two fragments (surface plus oligomer) together, and has only a minor dependence on the size of the oligomer. Most of the entropic change corresponds to the conversion of translational and rotational degrees of freedom in the separate fragments to vibrational degrees of freedom in the adsorbed species, and this has little dependence on the size of the system. It follows that the interaction free energy of a monomeric complex with the surface would be approximately +2 kcal/mol (-15 plus 17 kcal/mol), therefore non-binding. Thus, the large number of small binding interactions generates a very strong attachment of the polymer to the surface with the binding energy increasing as the length of the polymer chain increases as well. Our calculations are carried out in vacuum and thus offer an approximate value for the binding energy, since solvent effects with explicit molecules have not been taken into consideration. However, these calculations provide a good model for the experimental effects observed in this particular system
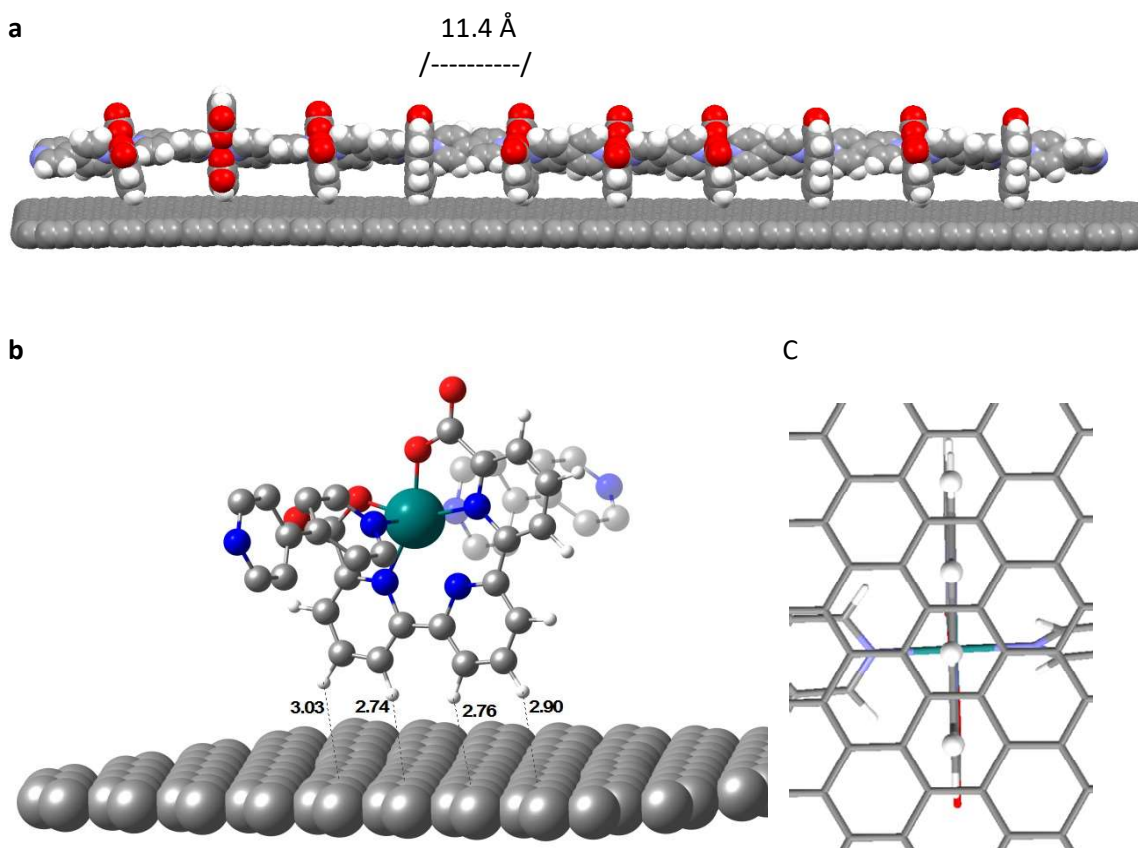
Fig. 4. **a**, Space fill representation of the DFT calculated structure of **10** anchored on a graphene surface. **b**, ball and stick representation of the interaction of one of the Ru fragments of **10**, with the graphene surface showing the CH-π bonding distances. **c**, Detail of the capped sticks representation of the structure shown in B, viewed from the back side. The interacting Ru-tda H-atoms with the graphene surface are depicted as white balls. Color code: Ru, green; O, red; N, blue; C, gray; H, white.

It is worth mentioning here that the high affinity of **15** for graphitic surfaces also enable a larger surface coverage in comparison to other anchoring strategies for related complexes described in the literature. For instance, the surface coverage of a **GC** disk by **15** is approximately 75%, thus below a monolayer, as deduced from electrochemical experiments (see Supplementary Fig 2), that will be further discussed in the next section. In the case of the CNT, the surface coverage in **15@CNT** in terms of Ru centers per surface area is about 2-5 times larger than in the cases of mononuclear Ru-tda complexes while using pyrene as an anchoring functionality as is the case for [Ru(O)(tda)(pyp)$_2$],

1-O-pyp, or [Ru(O)(tda)(pypA)$_2$], **1-O-pypA**, (pypA is 4-(pyren-1-yl)-N-(pyridin-4-ylmethyl)butanamide) (see Supplementary Fig 26).[28]

In comparison to other mononuclear complexes with a phosphonate functionality bonded to an oxide containing surface, the new Ru oligomers generate surface coverages that are about 10-100 times higher[52] depending on the oxide surfaces, thus clearly manifesting the convenience and effectiveness of the CH-π strategy described here (see Supplementary Table S2).

With the aim to further spectroscopically characterizing these hybrid materials, X-ray absorption near edge structure (XANES) and extended X-ray absorption fine structure (EXAFS) spectra were performed for **15** as a powder and attached to the surface of MWCNT deposited onto a glassy carbon plate (**GC$_p$**), **15@CNT@GC$_p$** and are reported in Fig. 5. The inset of Fig. 5a shows the half-edge energies obtained from XANES and reveals that while **15** remains at oxidation state +II as a powder, it is oxidized all the way to 96% Ru(III) with only 4% remaining as Ru(II) upon anchorage onto the surface of a MWCNT and exposure to atmospheric oxygen. We label this new material as **15@CNT@GC$_p$**'. This phenomenon was also observed for a related mononuclear Ru-tda complex, **1-pypA@CNT**,[28] and manifests the facility of oxidation of highly dispersed complexes adsorbed at the surface of graphite by dioxygen in the air. The experimental and simulated EXAFS spectra carried out for **15** and the partially oxidized **15@CNT@GC$_p$**' material, are shown in Fig. 5a and the SI (see Supplementary Fig. 32 and Supplementary Tables 3-5) and agree with a typical octahedral coordination for Ru(II) in **15** as well as for the Ru center in **15@CNT@GC$_p$**'. An additional contact distance at ~2.35 Å (Supplementary Tables 4 and 5) is moreover observed for the **15@CNT@GC$_p$**' complex associated with the dangling carboxylate group, in a similar manner as was previously observed for the reference mononuclear [Ru^{III}(tda)(py)$_2$]$^+$ complex.[28]
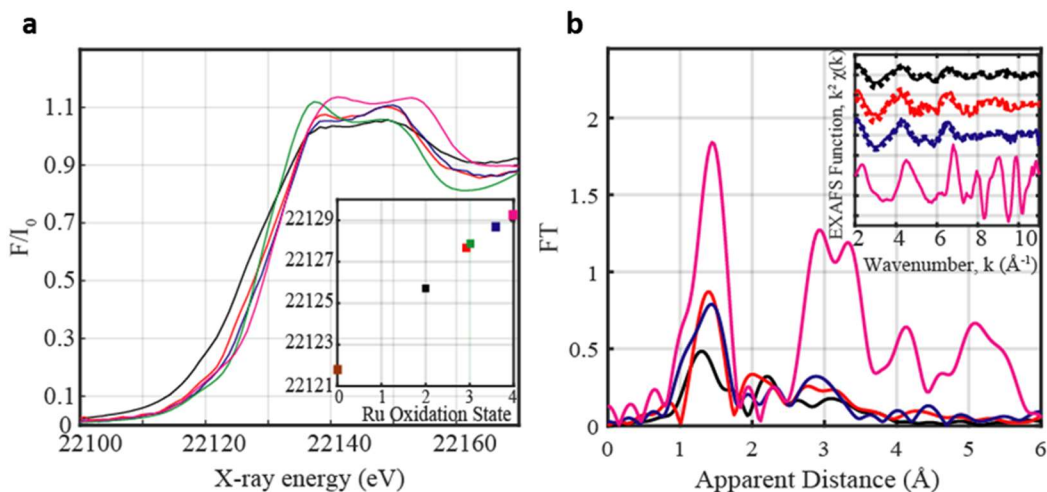
Fig. 5. **a**, Normalized Ru K-edge XANES for **15** (black), **15@CNT@GC$_p$$'$** (red), [Ru^{III}(tda)(py)$_2$]$^+$ (green), **15-O@CNT@GC$_p$** (blue) and RuO$_2$ (magenta). Inset, plot of half peak k-edge energy *vs*. oxidation state including Ru^0 (brown) collected from a Ru metal calibration foil. **b**, Fourier transforms of k^2-weighted Ru EXAFS. Inset**,** back Fourier transformed experimental (solid lines) and fitted (dashed lines) k^{2}χ(k) for Ru complexes together with RuO$_2$. Experimental spectra were calculated for *k* values of 1.941-11 Å^{-1}. Same color code as in left.

Water oxidation electrocatalytic performance.

The [Ru(O)(tda)(py)$_2$], **1-O-py**, complex represents the best water oxidation catalyst reported so far in terms of TOF[45] in homogeneous phase. The catalytic pathway undergone by **1-O-py** follows a water nucleophilic attack (WNA) O-O bond formation mechanism. For these two facts, it constitutes one of the best candidates for surface anchorage for the generation of highly efficient electro- and photo-anodes. Indeed, the anchoring of **1-O-pypA** on MWCNT generate highly efficient electroanodes after drop casting on glassy carbon electrodes (GC), **1-O-pypA@CNT@GC**, for the water oxidation reaction as has been recently described.[28] The anchoring was hereby achieved via pyrene functionalization and even though it resulted in a very stable WO electroanode, the current densities obtained were in the 5-10 mA/cm^2 range that are still far from the ones operating in commercial electrolyzers typically ranging from 0.2-1.0 A/cm^2.[35,36]

Thanks to its high affinity for graphitic surfaces, the present oligomers **n@CNT** are expected to generate unique electroanodes due to both the enhancement of surface coverages and the enormously improved stability thanks to the nature of the novel anchoring interactions that

provides a reversible CH-π bond breaking and forming scenario. The electrochemical properties of the **n@CNT** materials were evaluated based on CV and bulk electrolysis techniques. Figure 6 shows the CV of the **15@CNT** deposited onto the surface of glassy carbon electrode via drop casting, labeled here as **15@CNT@GC** (see Supplementary Information for the protocols used here for related electrochemical properties displayed by **5@CNT@GC**; Supplementary Fig. 24). As shown in Fig. 6 two one-electron redox process are observed at $E_{1/2}$= 1.06 V (ΔE = 45 mV) and $E_{1/2}$= 1.51 V (ΔE = 70 mV) due to the Ru(III/II) and Ru(IV/III) couples, respectively (all redox potentials are reported vs. RHE). The redox potentials obtained here are very similar to those obtained for the monomer **1** in homogenous solution at the same pH, and thus suggests that each individual Ru center of the polymer acts in a similar manner as in the discrete mononuclear complex. This is a consequence of the anchoring nature of the polymer at MWCNT, whereby each metal center has the same access to the surface thus facilitating a synchronized electron transfer process to the electrode. These **n@CNT** hybrid materials are used as precursors to generate the corresponding Ru-OH$_2$ complexes, denoted here as **n-H₂O@CNT**, and are actually the species providing access to the water oxidation catalytic cycle.

To generate **15-H₂O@CNT@GC**, the precursor complex **15@CNT@GC** is exposed to an applied potential E_{app} = 1.96 V for 16 minutes in a pH 12 phosphate buffer (phbf) solution followed by a E_{app} = 0.71 V for 30 seconds. The hybrid electrode is afterwards rinsed with water and placed again in a pH 7 solution (see additional details of this protocol in Supplementary Information). Figure 6 shows the CV of **15-H₂O@CNT@GC**, where two new waves due the Ru(III/II) and Ru(IV/III) electron transfers at 0.60 and 0.90 V are observed. The initial waves due to the precursor complex have disappeared thus indicating a complete conversion from the precursor complex to the corresponding Ru-OH$_2$ species. Related experiments can be carried out using **15** anchored on **GC** disk, **15@GC**. It is striking to see that the performance of the activated new hybrid material **15-H₂O@GC** is practically identical to that of **15-H₂O@CNT@GC** when normalized by the number of active Ru centers and thus points out that the main role of the **CNT** is to increase the overall mass of catalyst on the electrode surface (See Supplementary Fig. 29).

The total transformation of the precursor complex **15**, into the catalytically active species in the **CNT** is in sharp contrast to the behavior of the **1-O-pypA@CNT** homologue where the ratio of precursor *vs*. activated complex is at approximately 2:1.[28] The ratio of activated *vs*. precursor reflects the capacity of the dangling carboxylate to coordinate back to the metal center and eject the

17

coordinated aquo group from the first coordination sphere of the metal center. This equilibrium is clearly affected by the packing organization of the anchored oligomers and the proximity of the Ru-aqua active site to the surface of the electrode.

The supramolecular interaction among neighboring polymer units through hydrogen bonding with water molecules can also influence the relative strength of interactions between the intramolecular carboxylate coordination and the Ru-aqua formation (Supplementary Fig. 41), and is thus responsible for the activity of **15-H₂O@CNT@GC** over the whole 0-14 pH range (Supplementary Fig. 27). In sharp contrast its monomeric counterpart in homogeneous phase is only active above pH 5.5.[45]
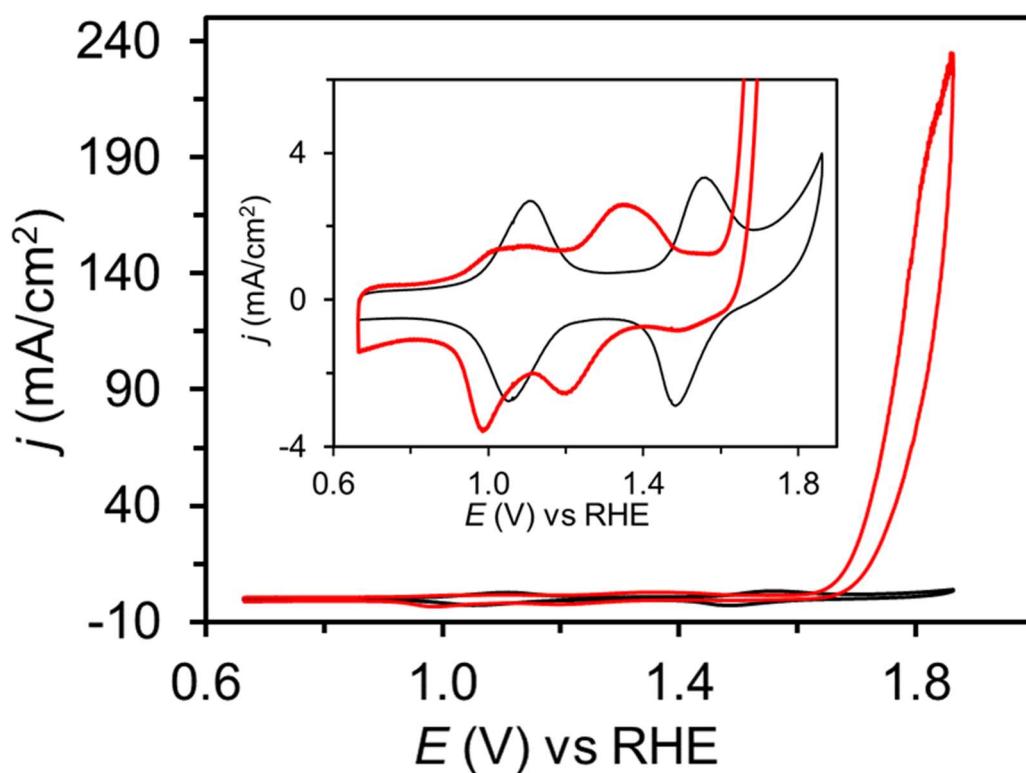

Fig. 6. CV of **15@CNT@GC** (black line) and **15-H₂O@CNT@GC** (red line) with a surface coverage of 17.7 nmol·cm^{-2} in 1.0 M phosphate buffer (pH 7) at scan rate of 100 mV/s. Inset, enlargement of the non-catalytic redox waves.

At higher anodic potentials, a large current is observed due to the electrocatalytic oxidation of water to dioxygen whose onset is at 1.61 V and that reaches unprecedented current densities for molecular based hybrid electrodes up to 240 mA/cm^2 at 1.86 V (Fig. 6).The current density obtained here is about 20 times larger than the highest current densities reported for **1-O-pyp@CNT** and is about two orders of magnitude larger than that of any other molecular catalyst anchored on an electrode surface (see Supplementary Table 2a).

FOWA analysis yield TOF$_{max}$ in the range of 8.000 s^{-1} (see Supplementary Fig. 31) which are very similar to those obtained in homogeneous phase for **1-py**[45] as are their respective Tafel plots (see Supplementary Fig. 28) and that further corroborates the molecular nature of the active species.

Bulk electrolysis experiments were carried out at 1.86 V for **15-H$_2$O@CNT@GC**. Impressively, the complex sustained current densities of 32 mA/cm^2 for 12 hours with practically no decay and generated overall TONs of ~2x10^5, (see Supplementary Fig. 25) yielding Faradaic efficiencies above 99% (Supplementary Fig. 30), thus highlighting the remarkable performance of these new hybrid molecular electroanodes (see Supplementary Fig. 25). Similar experiments carried out with **5@CNT** drop casted to a glassy carbon disks, **5-H$_2$O@CNT@GC**, showed comparable electrochemical behavior and stability as evidenced by CVs (see Supplementary Fig. 24).

Finally, XAS spectroscopy further provides here an excellent platform to evaluate the fate of the catalysts after turnover in the solid state. For this purpose, bulk electrolysis experiments were carried out using **15@CNT@GC$_p$** under similar conditions as the ones described previously but without the reduction process thus generating **15-O@CNT@GC$_p$**. Half-edge energies obtained from XANES for **15-O@CNT@GC$_p$**, reveal the presence of 59% Ru(IV) and 41% Ru(III) that is associated with the catalytic species containing the Ru(IV)=O and Ru(III)-OH groups respectively. Furthermore the EXAFS shown in Figure 5b display an increase in amplitude of the first coordination sphere that is associated with an increase in the Ru coordination number, from 6 to 7 together with the presence of a shortened Ru=O distance at ~1.64 Å, as expected for these types of complexes at oxidation state IV (see Fig. 5b and Supplementary Tables 3 and 4).[28,7] Significantly and importantly, XAS spectroscopy unambiguously showed the absence of any traces of RuO$_2$ after catalysis. This can be perceived from the absence of RuO$_2$ features in the EXAFS spectra shown in Figure 5b and Supplementary Fig. 32, clearly demonstrating the molecular nature of the whole catalytic process.

Conclusion

The judicious choice of solvent and relative ratios of starting Ru complex and bridging ligand together with column chromatography enables the isolation of pure samples of coordination oligomers with the desired number of repetitive units, up to 15. A new unique and convenient anchoring strategy using simultaneous and concurrent dynamic aromatic-CH-π interactions provides an extremely robust and easy heterogenization strategy for these coordination oligomers onto graphitic surfaces. This allows large surfaces coverages that are between one and two orders of magnitude larger than conventional pyrene or phosphonates functionalities for graphitic and oxide surfaces respectively. These new hybrid materials behave as extremely active electroanodes for the water oxidation reaction, delivering very high current densities that are unprecedented for this class of materials at neutral pH.

The present work provides the basis and principles for the design of extremely robust and efficient hybrid molecular electroanode materials for the oxidation of water to dioxygen based on Ru complexes, that can be potentially extended to other transition metals and other catalytic reactions.

Supplementary Information

Experimental details together with additional, analytic, spectroscopic, electrochemical, X-ray diffraction and DFT data.

Crystal Data Deposition: The crystal data parameters of **1** and **2** and all information related to the structures can be found in the deposited CIF/Checkcif-files. CCDC 1945004 (**1**) and 1945005 (**2**) contains the supplementary crystallographic data for this paper. These data can be obtained free of charge from The Cambridge Crystallographic Data Centre via www.ccdc.cam.ac.uk/structures.

REFERENCES

[1] Blakemore, J. D., Crabtree, R. H. & Brudvig, G. W. Molecular catalysts for water oxidation. *Chem. Rev.* **115**, 12974-13005 (2015).

[2] Berardi, S. *et al.* Molecular artificial photosynthesis. *Chem. Soc. Rev.* **43**, 7501-7519 (2014).

[3] Garrido-Barros, P., Gimbert-Suriñach, C., Matheu, R., Sala, X. & Llobet, A. How to make an efficient and robust molecular catalyst for water oxidation. *Chem. Soc. Rev*. **46**, 6088-6098 (2017).

[4] Matheu, R. *et. al.* The development of molecular water oxidation catalysts. *Nat. Rev. Chem.* **3**, 331-341 (2019).

[5] Duan, L. *et. al.* A Molecular ruthenium catalyst with water-oxidation activity comparable to that of photosystem II. *Nat. Chem.* **4**, 418-423 (2012).

[6] Suga, M. *et. al.* Native structure of photosystem II at 1.95 Å resolution viewed by femtosecond X-ray pulses. *Nature,* **517**, 99-103 (2015).

[7] Matheu, R., Ertem, Z. M., Gimbert-Suriñach, C., Sala, X. & Llobet, A. Seven coordinated molecular ruthenium-water oxidation catalysts: A coordination chemistry journey. *Chem. Rev*. **119**, 3453-3471 (2019).

[8] Garrido-Barros, P. *et. al.* Redox non-innocent ligand controls water oxidation overpotential in a new family of mononuclear Cu-based efficient catalysts. *J. Am. Chem. Soc.* **137**, 6758–6761 (2015).

[9] Grätzel, M. Artificial Photosynthesis: Water Cleavage into Hydrogen and Oxygen by Visible Light. *Acc. Chem. Res.* **14**, 376-384 (1981).

[10] Toshima, N. & Yonezawa, T. Bimetallic nanoparticles-novel materials for chemical and physical applications. *New J. Chem*. **22**, 1179-1201 (1998).

[11] Cao, S., Tao, F., Tang, Y., Lia, Y. & Yu, J. Size- and shape-dependent catalytic performances of oxidation and reduction reactions on nanocatalysts. *Chem. Soc. Rev.* **45**, 4747-4765 (2016).

[12] Kotani, H., Hanazaki, R., Ohkubo, K., Yamada, Y. & Fukuzumi, S. Size- and shape-dependent activity of metal nanoparticles as hydrogen evolution catalysts: Mechanistic insights into photocatalytic hydrogen evolution. *Chem. Eur. J.* **17**, 2777- 2785 (2011).

[13] Roy, C. *et. al.* Impact of nanoparticle size and lattice oxygen on water oxidation on $NiFeO_xH_y$. *Nat. Catal.* **1**, 820-829 (2018).

[14] Francàs, L. *et. al.* Ru–bis(pyridine)pyrazolate (bpp)-based water-oxidation catalysts anchored on TiO_2: The importance of the nature and position of the anchoring group. *Chem. Eur. J.*, *22*, 5261-5268 (2016).

[15] Hyde, J. T. *et. al.* Electrochemical Instability of Phosphonate-Derivatized, Ruthenium(III) Polypyridyl Complexes on Metal Oxide Surfaces., *ACS Appl. Mater. Interfaces.* **7**, 9554-9562 (2015).

[16] Wadsworth, B. L., Beiler, A. M., Khusnutdinova, D., Jacob, S. I. & Moore, G. F. Electrocatalytic and Optical Properties of Cobaloxime Catalysts Immobilized at a Surface-Grafted Polymer Interface *ACS Catal.* **6,** 8048-8057 (2016).

[17] Chen, Z., Concepcion, J. J., Jurss, J. W. & Meyer, T. J. Single-Site, Catalytic Water Oxidation on Oxide Surfaces. *J. Am. Chem. Soc.* **131**, 15580–15581 (2009)

[18] Ashford, D. L. *et. al.* Molecular Chromophore-Catalyst Assemblies for Solar Fuel Applications. *Chem. Rev.* **115**, 13006-13049 (2015).

[19] Wu, L. *et. al.* A Molecular Silane-Derivatized Ru(II) Catalyst for Photoelectrochemical Water Oxidation. *J. Am. Chem. Soc.*, **140**, 15062-15069 (2018)

[20] Kaminsky, C. J., Wright, J. & Surendranath, Y. Graphite-Conjugation Enhances Porphyrin Electrocatalysis. *ACS Catal.* **9**, 3667-3671 (2019).

[21] Jackson, M. N. *et. al.* Strong Electronic Coupling of Molecular Sites to Graphitic Electrodes via Pyrazine Conjugation. *J. Am. Chem. Soc.* **140**, 1004-1010 (2018).

[22] Oh, S., Gallagher, J. R., Miller, J. T. & Surendranath, Y. Graphite-Conjugated Rhenium Catalysts for Carbon Dioxide Reduction. *J. Am. Chem. Soc.* **138**, 1820-1823 (2016).

[23] Blakemore, J. D., Gupta, A., Warren, J. J., Brunschwig, B. S. & Gray, H. B. Noncovalent Immobilization of Electrocatalysts on Carbon Electrodes for Fuel Production. *J. Am. Chem. Soc.* **135***,* 18288-18291 (2013).

[24] Sheehan, S. W. *et. al.* A molecular catalyst for water oxidation that binds to metal oxide surfaces. *Nat. Commun.*, **6**, 6469 (2015).

[25] Mitchell, S., Thomas, J. M. & Pérez-Ramírez, J. Single atom catalysis. *Catal. Sci. Technol*., **7**, 4248-4249 (2017).

[26] Sala, X. *et. al.* Molecular Water Oxidation Mechanisms Followed by Transition Metals: State of the Art. *Acc. Chem. Res*. **47**, 504-516 (2014).

[27] Garrido-Barros, P., Matheu, R., Gimbert-Suriñach, C. & Llobet, A. Electronic, mechanistic and structural factors that influence the performance of molecular water oxidation catalysts anchored on electrode surfaces. *Curr. Opin. Electrochem.,* **15**, 140-147 (2019).

[28] Creus, J. *et. al.* A Million Turnover Molecular Anode for Catalytic Water Oxidation. *Angew. Chem. Int. Ed*. **55**, 15382-15386 (2016).

[29] McCrory, C. C. L., Jung, S, Peters, J. C. & Jaramillo, T. F. Benchmarking Heterogeneous Electrocatalysts for the Oxygen Evolution Reaction. *J. Am. Chem. Soc*, **135**, 16977-16987 (2013).

[30] McCrory, C. C. L. *et. al.* Benchmarking Hydrogen Evolving Reaction and Oxygen Evolving Reaction Electrocatalysts for Solar Water Splitting Devices. *J. Am. Chem. Soc.* **137**, 4347-4357 (2015).

[31] Smith, D. L. *et. al.* Photochemical route for accessing amorphous metal oxide materials for water oxidation catalysis. *Science*. **340**, 60-63 (2013).

[32] Merrill, M. D. & Dougherty, R. C. Metal oxide catalysts for the evolution of O_2 from H_2O. *J. Phys. Chem. C*. **112**, 3655-3666 (2008).

[33] Smith, R. D. L., Prevot, M. S., Fagan, R. D., Trudel, S. & Berlinguette, C. P. Water oxidation catalysis: electrocatalytic response to metal stoichiometry in amorphous metal oxide films containing iron, cobalt, and nickel. *J. Am. Chem. Soc.* **135**, 11580-11586 (2013).

[34] Salvatore, D. A., Pena, B., Dettelbach, K. E., and Berlinguette, C. P. Photodeposited ruthenium dioxide films for oxygen evolution reaction electrocatalysis. *J. Mater. Chem. A*, **5**, 1575-1580 (2017).

[35] Carmo, M., Fritz, D. L., Mergel, J. & Stolten D. A comprehensive review on PEM water electrolysis. *J. Hydrogen Energy*, **38**, 4901-4934 (2013).

[36] Zeng, K. & Zhang, D. Recent progress in alkaline water Electrolysis for hydrogen production and applications. *Prog. Energy Combust. Sci.* **36**, 307-326 (2010).

[37] Xu, J. *et. al.* Cluster beam deposition of ultrafine Cobalt and Ruthenium clusters for efficient and stable oxygen evolution reaction. *ACS Appl. Energy Mater.*, **1**, 3013–3018 (2018).

[38] Li, W. *et. al.* From water reduction to oxidation: Janus Co-Ni-P nanowires as high-efficiency and ultrastable electrocatalysts for over 3000 h water splitting. *J. Power Sources*, **330**, 156-166 (2016).

[39] Kanan, M. W. & Nocera, D. G. In situ formation of an oxygen-evolving catalyst in neutral water containing phosphate and Co^{2+}. *Science*. **321**, 1072-1075 (2008).

[40] Surendranath, Y., Kanan, M. W. & Nocera, D. G. Mechanistic Studies of the Oxygen Evolution Reaction by a Cobalt-Phosphate Catalyst at Neutral pH. *J. Am. Chem. Soc.* **132**, 16501-16509 (2010).

[41] Hoffman, R. E. Self-diffusion measurements of polycyclic aromatic hydrocarbon alkali metal salts. *J. Chem. Soc., Perkin Trans.* **2**, 1659-1664 (1998).

[42] Liu, T. & Xiao, Z. Dynamic light scattering of rigid rods – A universal relationship on the apparent diffusion coefficient as revealed by numerical studies and its use for rod length determination. *Macromol. Chem.* Phys. **213**, 1697–1705 (2012).

[43] Ma, J. et al., Amorphous FeNi-bimetallic infinite coordination polymers as advanced electrocatalysts for the oxygen evolution reaction*Chem. Commun.*, **55**, 12567-12570 (2019).

[44] (a) Bhunia, S. *et. al.* Efficacious Electrochemical Oxygen Evolution from a Novel Co(II) Porphyrin/Pyrene-Based Conjugated Microporous Polymer. *ACS Appl. Mater. Interfaces*, **11**, 1520–1528 (2019); (b) Zheng, T. & Li, L. {[Ru(bda)]$_x$L$_Y$}n cross-linked coordination polymers: toward efficient heterogeneous catalysis for water oxidation in an organic solvent-free system. *New J. Chem.*, **42**, 2526-2536 (2018); (c) Gong, Y.; Shi, H.-F.; Hao, Z.; Sun, J.-L. & Lin, J.-H. Two novel Co(II) coordination polymers based on 1,4-bis(3-pyridylaminomethyl)benzene as electrocatalysts for oxygen evolution from water. *Dalton Trans.*, **42**, 12252-12259 (2013). (d) Bhat, S. A.; Das, C. & Maji, T. K. Metallated azo-naphthalene diimide based redoxactive

porous organic polymer as an efficient water oxidation electrocatalyst. *J. Mater. Chem. A*, **6**, 19834-19842 (2018); (e) Zhao, S. *et. al.* Ultrathin metal-organic framework nanosheets for electrocatalytic oxygen evolution. *Nature Energy*, **1**, 16184 (2016).

[45] Matheu, R. *et. al.* Intramolecular Proton Transfer Boosts Water Oxidation Catalyzed by a Ru Complex. *J. Am. Chem. Soc.* **137**, 10786-10795 (2015).

[46] Neel, A. J., Hilton, M. J., Sigman, M. S. & Toste, F. D. Exploiting non-covalent π interactions for catalyst design. Nature, **543**, 637-646 (2017).

[47] Nishio, M. The CH/π hydrogen bond in chemistry. Conformation, supramolecules, optical resolution and interactions involving carbohydrates. *Phys. Chem. Chem. Phys.* **13**, 13873-13900 (2011).

[48] Lu, X. & Xiao, Y. Morphology of organic photovoltaic non-fullerene acceptors investigated by grazing incidence X-ray scattering techniques. *Materials Today Nano*, **5**, 100030 (2019)

[49] Rodríguez-Guerra Pedregal, J. *et. al.* GARLEEK: Adding an Extra Flavor to ONIOM. *J. Comput. Chem*. **40**, 381-386 (2019).

[50] Álvarez-Moreno, M. *et. al.* Managing the Computational Chemistry Big Data Problem: the ioChem-BD Platform. *J. Chem. Inf. Model*., **55**, 95-103 (2015).

[51] Waters, M. L. Aromatic interactions in model systems. *Curr. Opin. Chem. Biol.* **6**, 736-741 (2002).

[52] Concepcion, J. J., Jurss, J. W., Hoertz, P.G. & Meyer, T. J. Catalytic and surface-electrocatalytic water oxidation by redox mediator–catalyst assemblies. *Angew. Chem. Int. Ed.* **48**, 9473-9476 (2009).